Acta Materialia 282 (2025) 120368

Contents lists available at ScienceDirect

Acta Materialia

journal homepage: www.elsevier.com/locate/actamat

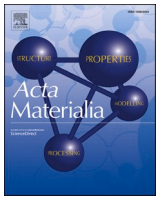

A level-set method for simulating solid-state dewetting in systems with strong crystalline anisotropy

Maxwell A. L'Etoile *, Carl V. Thompson, W. Craig Carter

Department of Materials Science and Engineering, Massachusetts Institute of Technology, Cambridge, MA 02139, USA

ARTICLE INFO

Keywords:
Solid-state dewetting
Level-set methods
Anisotropy
Single-crystal
Morphological evolution

ABSTRACT

Accurately modeling solid-state dewetting in materials with strong crystalline anisotropy is an open problem in materials science with importance for both the manufacturing and reliability of nano-scale devices. In this work, we propose and demonstrate a level-set method framework for simulating solid-state dewetting which is capable of modeling systems with strongly anisotropic surface energies and diffusivities. Surface energy anisotropy is handled through the use of the Cahn-Hoffman vector construction, and surface self-diffusivity anisotropy is handled through the use of a diffusivity tensor. We benchmark our method against isotropic phenomena with analytical descriptions and go on to demonstrate that our method is capable of reproducing a host of experimentally observed behaviors in strongly anisotropic single-crystal materials.

1. Introduction

Experimental observations reveal that many thin films attached to substrates such as metals on oxidized silicon, single crystal Si on SiO_2, and Ni on MgO or Sapphire, structures [1–6] are unstable with respect to islands of the thin film material. In general, the evolution of such systems toward stable configurations could be mediated by evaporation-condensation, volume diffusion, or surface self-diffusion [7]. However, experimental results in systems like those mentioned above often show that mass transport is dominated by surface self-diffusion [1–6,8–10]. Experiments also provide compelling evidence that crystalline anisotropy strongly influences this evolution [2–6, 8–12].

For large area films and other far from equilibrium features patterned from these films, this morphological evolution can be highly driven and give rise to various instabilities, including Rayleigh-like instabilities [13], a fingering instability [14,15], and a corner instability [9,16,17]. Accurately modeling the full continuum of dewetting behaviors, especially in systems with strong anisotropy, is an open problem in materials science.

If surface tension and surface diffusivity were isotropic, morphological evolution would be governed by the Mullins equation, which states that the velocity of evolving surfaces along their normal direction is proportional to the surface Laplacian of curvature [18]. As with other 4th order partial differential equations, traditional numerical methods for solving the Mullins equation require very small time steps to prevent numerical instability [19]. For crystalline films, anisotropy necessitates a reformulation of the Mullin's equation. In addition to facets, corners, and edges being non-differentiable, the chemical potential is not directly related to the geometric mean curvature [20]. Furthermore, anisotropic surface diffusivities require that the scalar surface diffusivity be replaced with a surface diffusivity tensor. Experimental observations of dewetting wires and films also show behaviors which include topological changes that are troublesome for Lagrangian front-tracking numerical methods.

A deeper understanding of the effects of crystalline anisotropy on solid state dewetting is important because of both the striking behaviors to which it gives rise and the impact these behaviors have on the use of dewetting to create intermediate structures for use in fabricating devices [8–10]. In anisotropic systems, retracting rims develop faceted profiles (see Fig. 1) [21], and small deviations in the alignment of patterned features relative to a film's crystalline axes can yield profoundly different behavior [13,15,22]. While this rich and complex behavior is of interest to both experimentalists and modelers, improved numerical methods are required to predict and understand these phenomena.

To this end, we present a level-set numerical approach for simulating the morphological evolution of anisotropic materials undergoing dewetting and surface diffusion mediated evolution driven by capillarity more generally. The method includes the effects of anisotropic surface energy and an anisotropic surface diffusion coefficient tensor. Our method reproduces experimental observations, including faceting and

* Corresponding author at: Aluminio Inc., 611 Taylor Way STE 1, San Carlos, CA, 94070, USA.
E-mail address: mletoile@alum.mit.edu (M.A. L'Etoile).

https://doi.org/10.1016/j.actamat.2024.120368
Received 19 May 2024; Received in revised form 24 August 2024; Accepted 4 September 2024
Available online 11 September 2024

topological transitions. We have also tested our method in the absence of anisotropy and show that we can reproduce previous analytical, numerical, and computational results. Example simulations using this code are openly available on Github [71].

2. Background

For isotropic systems, there are many examples of modeling behavior governed by the Mullins equation. Mullins' equation was initially applied to grain boundary grooving [18] and the evolution of surfaces of revolution [23,24], including Rayleigh instabilities [25], which have since been modeled in more complex systems such as materials in contact with a substrate [26] and materials constituting an intragranular phase [27]. Brandon and Bradshaw [1] conducted early work on solid-state dewetting, in which they developed a simple analytical model in which a straight dewetting edge's retraction distance scales with $t^{2/5}$. Computational [21,28,29] and experimental [12,14] work reproduced approximate $t^{2/5}$ scaling at sufficiently long times. Nichols later showed that finite cylinders are also prone to ovulation [30]—the repeated pinching off and spheroidization of a cylinder's ends—in addition to the Rayleigh instability. Smereka developed a level-set method to model evolution mediated by surface self-diffusion in isotropic systems, but did not model interactions with substrates [19]. Jiang et al. also conducted phase-field simulations of several isotropic solid-state dewetting phenomena [31].

Other approaches that go beyond the direct application of the Mullins equation are needed for anisotropic surface energies. The "crystalline method" enables modeling evolution through the movement, creation, and annihilation of facets in fully-faceted systems [32–34]. This method has been used to study edge retraction in fully faceted systems, including the effects of assigning different diffusivities to different facets [21]. Dornel et al. constructed an anisotropic extension to the method in Ref. [28] and explored edge retraction behavior in Si films [35]. Burger et al. utilized anisotropy in level-set method simulations [36]. Jiang et al. simulated anisotropic dewetting using a finite-element method [37,38] and Pierre-Louise et al. used a Kinetic Monte Carlo (KMC) method to simulate dewetting [39–41]. Kim and Thompson used KMC to study the orientational dependence of single-crystal nanowire stability [13]. The $\overrightarrow{\xi}(\hat{n})$-construction (described below) was used in reference [36], which took a variational level-set approach to modeling both mean curvature flow and surface diffusion (though not dewetting, as there was no substrate in their systems) and in [37,38], which use finite-element methods to model anisotropic dewetting. Both methods demonstrated simulations with regularized hard surface energy anisotropy, though neither placed emphasis on using $\gamma(\hat{n})$ derived from real physical systems. However references [37,38] provide many examples using technologically relevant geometries, including long wires and edges. Wang and Karma [42] studied the stability of faceted crystalline wires using the Phase Field (PF) method, showing that such wires can be susceptible to a finite-amplitude, nonlinear instability. All the methods described above have specific strengths and drawbacks and are each best-suited to particular classes of problems. In general, the crystalline method works well for modeling the behavior of fully-faceted systems, but is unable to model systems which contain any rounded edges or corners. Finite element methods work well for a large set of geometries and material properties but can't easily capture topological changes such as hole formation or wire fragmentation without addressing them on a case-by-case basis. KMC naturally handles all topology changes, and geometric features emerge from the arrangement of the atoms in the simulation. However, KMC is quite computationally intensive, and it can be difficult to map macroscopic material properties, such as surface energy and diffusivity, into the atomistic KMC model. PF simulations share many of the same strengths as those employing LSM, including implicit handling of topological changes and the ability to use macroscopic material properties in the model. PF models can also make use of Lagrange multipliers to enforce volume conservation [42], while more elaborate approaches have been required to achieve strict volume conservation in LSM simulations [43–45]. However, PF models make use of a diffuse interface which makes it more difficult to model sharp edges and corners, in comparison to LSM models. As detailed below, we were able to employ numerical techniques in our LSM simulations to significantly, though not completely, mitigate traditional volume

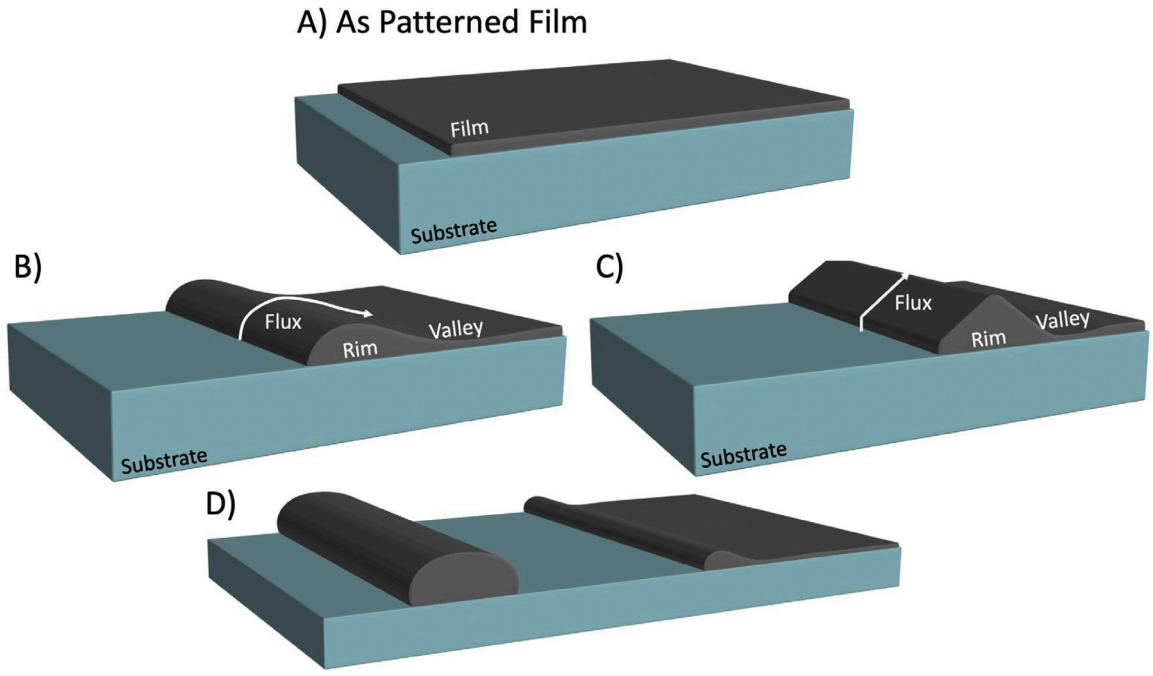

Fig. 1. Schematic illustration of retraction of a film edge in isotropic and strongly anisotropic films. Material dewetted from the substrate accumulates in a rim that propagates into the film. A) The as-patterned film. B) Intermediate dewetting morphology for an isotropic system. C) The same intermediate morphology for a simple anisotropic system. D) An isotropic system which has dewetted to and through the point of pinch-off. In isotropic systems, a valley always forms behind the rim while the extent of valley formation in anisotropic systems is determined by material properties. This will be discussed at greater length later in the text.

conservation issues with LSM while retaining the ability to model sharp interfaces, making LSM a compelling choice for modeling solid-state dewetting.

In the absence of other potentials, surface self-diffusion is driven by gradients in weighted mean curvature (κ_γ), and the Mullins equation becomes $v_n = \nabla_s \cdot \left(D(\hat{n}) \frac{\nu \Omega^2}{k_B T} \nabla_s \kappa_\gamma \right)$, where $D(\hat{n}) = R^T(\hat{n}) D(\hat{n})_{\text{natural}} R(\hat{n})$ for D_{natural} of the form $\begin{matrix} d_1 & 0 & 0 \\ 0 & d_2 & 0 \\ 0 & 0 & 0 \end{matrix}$ for an orthonormal basis $\hat{v}_1, \hat{v}_2, \hat{n}$ and an appropriate change of basis matrix $R(\hat{n})$. In practice, we lump all the materials properties together and use an equation of the form $v_n = \nabla_s \cdot \left(B(\hat{n}) \nabla_s \kappa_\gamma \right)$, where $B(\hat{n})$ incorporates anisotropic diffusivity. Taylor [20] defines κ_γ as "the rate of decrease of surface free energy with respect to volume swept out by the motion of the surface." There are several mathematically equivalent formulations of κ_γ, of which Taylor [20] gives an exhaustive review, but the formulation of κ_γ used throughout this work is the divergence of the Cahn-Hoffman vector $\vec{\xi}(\hat{n})$, [46]. For an isotropic system, $\kappa_\gamma = \kappa = \nabla \cdot \vec{\xi}(\hat{n}) = \gamma \nabla \cdot \hat{n}$. The Cahn-Hoffman vector, commonly denoted as $\vec{\xi}(\hat{n})$, is the gradient of the homogeneous extension of the surface energy function $\Gamma(A\hat{n}) = A\gamma(\hat{n})$. Fig. 2 walks through this construction graphically. The vector components of $\vec{\xi}(\hat{n})$, $\{\xi_x, \xi_y, \xi_z\}$, are derivatives of a surface's free energy relative to changes of its area and orientation. These vector components are analogous to the chemical potentials of compounds in solution, which are derivatives of a solution's total free energy with respect to changes in the composition. This analogy is explored in detail in reference [47]. For a given $\gamma(\hat{n})$, the curve $\vec{\xi}(\hat{n})$ plotted for all surface orientations $\hat{n}$, contains the Wulff shape with the addition of "ears" or "swallowtails" for the unstable orientations, if there are any (i.e., the case of sharp edges on the Wulff shape), see Fig. 2(F). These ears are the orientation-space analog of a miscibility gap in alloys [47].

In simulations of systems with such unstable orientations, we use a Willmore regularization term [48] $-\varepsilon^2 \left(\kappa_{ss} + \frac{1}{2}\kappa^3 \right)$. This regularization appears to have first been proposed in this context in Ref. [49] and is used in many studies of anisotropic surface evolution including Refs. [36–38]. Refs [38,50] provide particularly clear explanations of this regularization. The regularization is the analog to the square-gradient term in diffuse-interface theories (e.g., Cahn-Hilliard [51] and Allen-Cahn [52] functionals). Without regularization, surfaces with unstable orientations would develop facets or pyramids of arbitrary—and possibly infinitesimal—length scale (i.e., varifolds [53]). We find that the magnitude of the regularization coefficient sets the length scale of the faceting instability in our simulations, as expected. In many of our simulations, we construct the convex portion of $\vec{\xi}(\hat{n})$ from an observed Wulff shape, and we find that the exact functional form of the non-convex parts of $\vec{\xi}(\hat{n})$ (i.e., the "ears") plays a very negligible role in the results.

Our simulations are based on the level-set method, an Eulerian approach for simulating the evolution of surfaces, developed by Osher and Sethian [54]. In the level-set method, the surface being simulated is the zero isocontour, or level-set, of a function $\phi(\vec{x})$ (usually chosen to be a signed distance function). Numerically, surface evolution is implemented by incrementally updating $\phi(\vec{x})$ by computing $\frac{\partial \phi}{\partial t} + \vec{v} \cdot \nabla \phi = 0$ for small time-steps (see Fig. 3). Level set methods are useful for studying morphological evolution, particularly when topological changes occur, as the implicit representation of the evolving surface naturally handles such changes without special treatment. Another

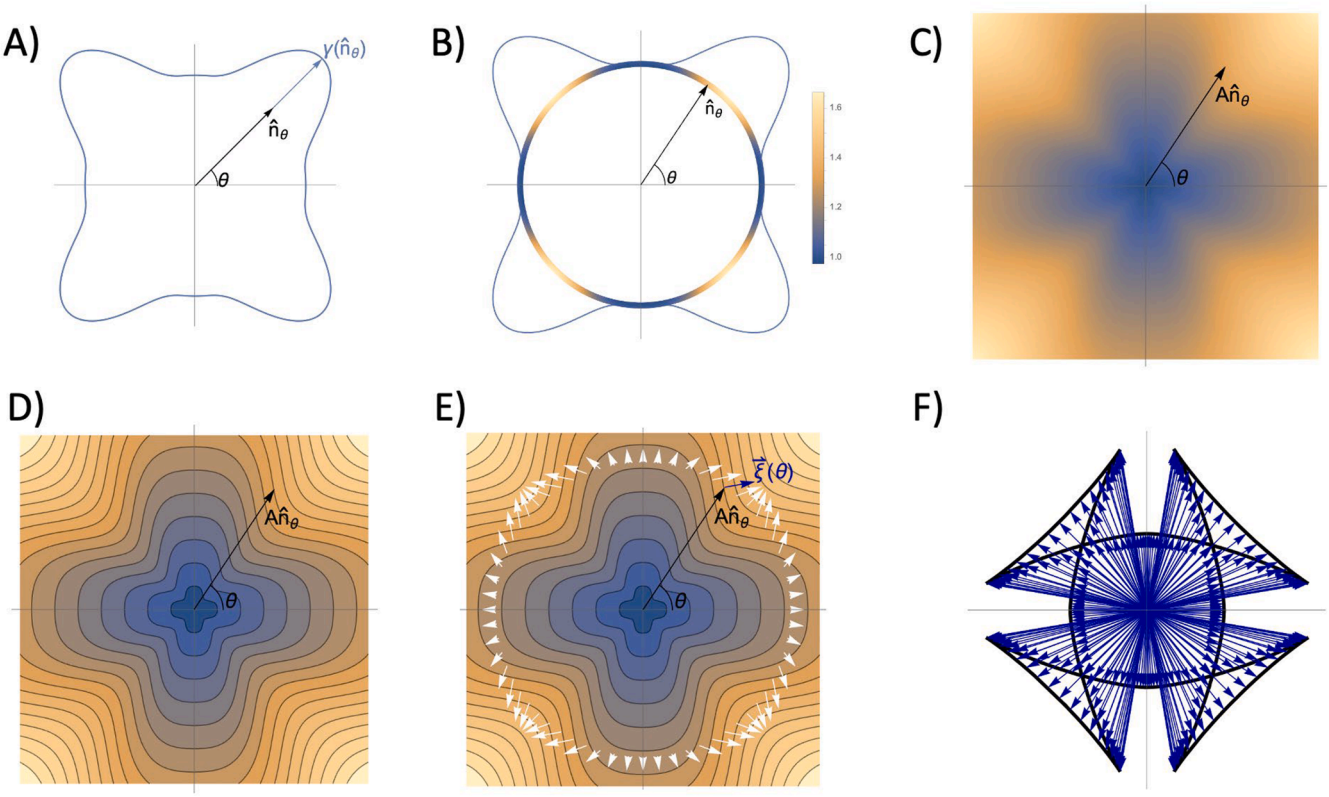

Fig. 2. The ξ-vector construction. From left to right, top to bottom: A) The surface energy function $\gamma(\hat{n})$ shown as a polar plot. B) An alternative representation as a scalar function on the unit circle. C) An extension of the scalar function over all space such that $\gamma(A\hat{n}) = A\gamma(\hat{n})$, D) $A\gamma(\hat{n})$ isocontours clarify where γ is changing most rapidly. E) White arrows indicate $\vec{\xi}(\vec{n})$ for $\hat{n}$ of magnitude 1, where $\vec{\xi}(\vec{n})$ is the gradient of $A\gamma(\hat{n})$. F) A plot of just $\vec{\xi}(\hat{n})$ from the origin, which yields the traditional ξ-vector construction. The convex portion of the black curve in F) is gives the equilibrium shape.

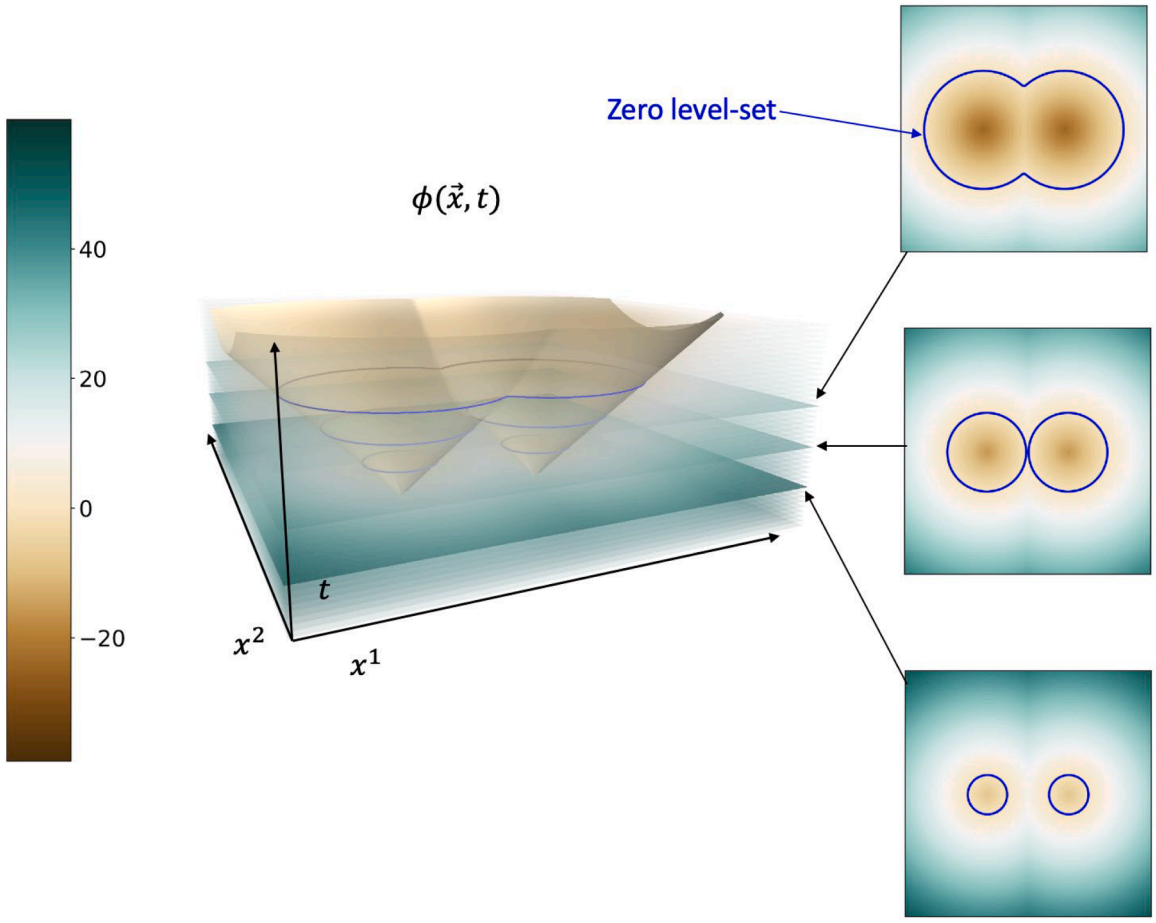

Fig. 3. The level-set method implicitly encodes the location of interfaces (indicated by the blue outlines) in the values of a signed distance function, $\phi(\vec{x},t)$. The magnitude of ϕ gives the distance from $\vec{x}$ to the closest interfacial point and the sign indicates whether $(\vec{x},t)$ is inside ($\phi(\vec{x},t)<0$) or outside ($\phi(\vec{x},t)>0$) an interface. Here, two neighboring circles grow and merge (right, bottom to top). The evolution of ϕ is shown in the center of the figure, with the time axis oriented vertically. Three Individual time steps are highlighted for clarity.

benefit is that geometric quantities, such as the normal vector and curvature, are naturally defined in terms of derivatives of $\phi(\vec{x})$. Naïve implementations of LSM are plagued by issues of stability and volume conservation arising from distortions to $\phi(\vec{x})$, which cause it to locally deviate from a signed distance function. Redistancing methods, which are used in our simulations and discussed in detail below, combat this problem by approximately restoring $\phi(\vec{x})$ to a signed distance function without moving the zero level-set. A complimentary approach described by Zhao et al. [55] and first implemented by Smereka [19] removes the distortionary components of calculated quantities, by solving $\frac{\partial g}{\partial t} + sign(\phi)\frac{\nabla\phi}{|\nabla\phi|}\cdot\nabla g$, where g can be any calculated quantity such as interface velocity or κ_γ.

3. Methods

For an LSM simulation of surface self-diffusion driven by the gradient of weighted mean curvature, the governing equation for the time-evolution of $\phi(\vec{x},t)$ is

$$\frac{\partial\phi}{\partial t} = -\left(\nabla_s\cdot\left(B(\hat{n})\nabla_s\kappa_\gamma\right)\right)\nabla\phi \ . \tag{1}$$

As discussed above, $B(\hat{n})$ incorporates the effect of anisotropic diffusivity, while κ_γ incorporates the effect of anisotropic surface energy. This equation is numerically integrated forward in time using finite differences. Conceptually, in fact, LSM simulations do nothing more than integrate this governing equation forward in time. However, in practice, numerically integrating this equation forward in time without performing additional operations, discussed below, quickly leads to numerical instabilities and poor volume conservation caused by unphysical distortions to $\phi(\vec{x})$. These distortions arise from erroneous values for physical quantities calculated away from the interface. For example, only the calculated values of κ_γ on the $\phi(\vec{x})=0$ level-set have physical meaning, and the $\phi(\vec{x})=5$ level-set will tend to have much different values of κ_γ. If the differing values of κ_γ on other level-sets, $\phi(\vec{x},t)\neq 0$, are not corrected, these level-sets won't move in sync with the zero-level-set, and $\phi(\vec{x},t)$ will become distorted, negatively impacting the accuracy of the simulation. We utilize the correction method developed by Smereka[19] and Zhao et al. [55]. This approach replaces non-interfacial values of both κ_γ and surface velocity with values obtained by extending the physically meaningful interfacial values out into a band of points encapsulating the interface. Smereka proposes a specific algorithm for performing this extension, but in our testing, we obtained better results using Adalsteinsson and Sethian's extension algorithm [56] based on the Fast Marching Method (FMM) [57]. In all of the work presented here, we used the implementation of Adalsteinsson and Sethian's algorithm found in the scikit-fmm Python package [58]. While these extension steps reduce unphysical distortions to $\phi(\vec{x})$, we also periodically redistanced $\phi(\vec{x})$ to reset it to a signed distance function. In our testing, we found that Sussman's redistancing method [59] usually yields the best results, as opposed to fast marching based redistancing, and the results presented here are all from simulations making use of

Sussman's method.

Numerically, we combine second order spatial derivatives with first order time stepping. Unfortunately, the central difference stencils used to compute $\nabla\phi(\vec{x})$, and thus $\hat{n}(\vec{x})$, yield the same normal vector for a flat surface and for a sawtooth surface with the same average orientation. During development, this led to non-physical oscillations developing on thermodynamically stable surfaces in some strongly anisotropic simulations. To combat this, we add a small term that goes as $\nabla^2\phi(\vec{x})$ to κ_γ, calculated using second-order central differences. This term is similar to the curvature of the surface, so setting it too large will cause non-physical smoothing in anisotropic systems. We still found this smoothing operator to yield superior results to that used in Ref. [19], which is non-local in nature and thus introduced clearly non-physical distortions in our testing; Ref. [19] acknowledges the problems posed by these distortions. To increase computational performance, the size of the time step taken for each iteration is adaptively determined by $\Delta t = \alpha\Delta x/|S|_{max}$, where Δx is the grid spacing, $|S|_{max}$ is the maximum of the absolute value of the interface velocity, and α is a scaling factor less than 1. In practice, good results are often obtained with $\alpha \approx 0.01$. In 3D simulations, we found the performance cost of redistancing after every iteration was outweighed by the larger α it allowed us to use, while in two dimensions, such frequent redistancing was not always necessary. We found that α having too large a value led to volume drifting upward while setting it too small led to downward volume drift. Therefore, in most simulations, we adjust α after each time step by a very small amount, negatively proportional to the preceding time step's change in volume as a percentage of the initial volume. We find that α tends to trend downward during periods of topological change, such as pinch-off or ovulation, and then rebound when evolution is less extreme. If α climbs to too high a value, the simulation can become unstable, and if it becomes too low, the simulation takes too long to run, so we also set upper and lower bounds on α. In simulations in which α was made adaptive in this way, changes in volume over the course of the simulation were often less than a percent, and no simulations presented here had volume changes greater than a few percent. In comparison to techniques that strictly enforce global volume conservation [42,43,60], our method for mitigating volume loss doesn't introduce non-diffusive mass transport, a criterion we prioritized over perfect global volume conservation. In fact, the authors of [42] note that their volume conservation constraint, "is used to avoid slow surface diffusion dynamics," which is beneficial for a stability analysis but would present problems for our application. For all volume measurements in this paper, we follow Sussman's use of a smoothed Heavyside function [59] to define the volume of a body characterized by a signed distance function. For more details on numerical implementation, see the appendix.

As discussed above, surface energy anisotropy is incorporated into the simulations through the Cahn-Hoffman vector $\vec{\xi}(\hat{n})$. For crystalline systems, calculating $\vec{\xi}(\hat{n})$ can be computationally expensive, so values of $\vec{\xi}(\hat{n})$ for such systems were precomputed and accessed via a lookup table. For 3D simulations, these lookup tables were generated using the method proposed in Smith et al. [61]. In 2D, we found that lookup tables with 10^3 to 10^5 points were sufficiently dense while in 3D, we used lookup tables with up to about 3×10^6 points for materials for which very small facets needed to be resolved. In 2D simulations, $\vec{\xi}(\hat{n})$ could also be interpolated between lookup values by fitting a spline to the whole lookup table. For simulations which sought to match the behavior of a specific material, an initial $\gamma(\hat{n})$ was created using DFT-calculated surface energies from Tran, et al. [62]. Non-equilibrium orientations could be treated in a variety of ways to tune the hardness of the anisotropy. In each case, the final $\gamma(\hat{n})$ was then extended and numerically differentiated to yield $\vec{\xi}(\hat{n})$, as detailed in the background section. In other cases, arbitrary functional forms of $\vec{\xi}(\hat{n})$ were created to explore how surface energy anisotropy affects dewetting-like processes more generally. For example, we conducted early simulations in a fictional simple cubic system with very high surface energy for all but {100} surfaces (i.e., the Wulff shape was a cube). For simulations of true dewetting (i.e. simulations in which the evolving material is in contact with a substrate), we initialize the simulation such that the zero level-set of $\phi(\vec{x})$ intersects the bounding box of the simulation domain along the $x = x_{max}$ plane. This means that the contact patch between the film and the substrate is implicitly represented by the triple-line. An additional plane of ghost values is maintained below the physically meaningful simulation domain, which helps to more accurately maintain the zero-flux boundary condition at the substrate. In the vicinity of the triple-line, these ghost values are set such that $\phi(y = y_{max} + 1) = \phi(y = y_{max}) + \frac{\partial\phi}{\partial y}|_{y=y_{max}}$. This approach is similar to that used in Ref. [63] but is distinct in that we do not force the system to have a specific contact angle. To correctly model the evolution of the triple-line, we set $\kappa_\gamma = \nabla\cdot\vec{\xi}(\hat{n}) + \left(\widehat{c_\Gamma^\gamma}\cdot\widehat{n_\Gamma} + \gamma_{FS} - \gamma_{VS}\right)\frac{\sqrt{n_x^2+n_z^2}}{\Delta x\sqrt{1+n_y^2}}$ for points in the $y = y_{max}$-plane in the vicinity of the triple-line, where $\widehat{c_\Gamma^\gamma} = \left(\vec{\xi}(\hat{n})\cdot\hat{n}\right)\widehat{c_\Gamma} - \left(\vec{\xi}(\hat{n})\cdot\widehat{c_\Gamma}\right)\hat{n}$, $\widehat{n_\Gamma}$ is the in-plane normal vector of the triple-line, and $\widehat{c_\Gamma}$ is the unit vector defined to be tangent to the evolving surface and orthogonal to the triple-line while being oriented such that it points toward the substrate. This is similar to Ref. [37] which derives that $\widehat{c_\Gamma^\gamma}\cdot\widehat{n_\Gamma} + \gamma_{FS} - \gamma_{VS}$ is the first variation of total free energy of the system with respect to displacement of the triple-line. In our level-set formulation, however, the triple-line is represented implicitly, so we incorporate this quantity into κ_γ, rather than treating the evolution of the triple-line separately, as is done in Ref. [37]. The geometric factor $\frac{\sqrt{n_x^2+n_z^2}}{\Delta x\sqrt{1+n_y^2}}$ relates the variation of the triple-line to the variation of the surface element directly above the triple-line. We apply zero-flux boundary conditions at the triple-line and, in 3D simulations, also prohibit flux along the triple-line.

4. Results

4.1. Isotropic systems

To benchmark our technique, we simulated edge retraction and the Rayleigh instability in isotropic systems and compared our results to theoretical and previous simulations. For the retraction of an isotropic, semi-infinite film, the retracting rim should develop a smooth profile composed of a "rim" containing most of the dewetted material followed by oscillations in film height of decaying amplitude; the first minimum is often referred to as the valley [28,35] (Fig. 3). Eventually this valley touches down to contact the substrate, separating the rim from the rest of the film in a behavior called pinch-off. Starting with an edge like the one shown in Fig. 1(A), the edge retraction distance initially increases rapidly but then is expected to evolve to approximately scale as $t^{2/5}$ [28,29]. This behavior in isotropic systems, as well as the effect of contact angle, is explored in depth in [28] and our simulation results match theirs (Figs. 4 and 5). We also report scaling relations for the valley depth and rim height which were not explicitly discussed in Refs. [28,35].

As a second test, we simulated Rayleigh-like instabilities [25] on free-standing cylinders with isotropic surface energy evolving by surface diffusion. Perturbations with wavelengths greater than the circumference of the wire will grow, eventually breaking the cylinder into spheres [24]. Our simulation technique reproduced the correct behavior with small wavelength ($\lambda < 2\pi R_0$) perturbations on infinite cylinders (modeled as finite segments with periodic boundary conditions) decaying to zero amplitude and perturbations with supercritical wavelengths ($\lambda > 2\pi R_0$) growing and breaking up the wire, see Fig. 6(A) and 6 (B). Perturbations close to $\lambda = 2\sqrt{2}\pi R_0$ grew the fastest, in correspondence to theory [24]. In Fig. 6(C), a long, finite wire was given an

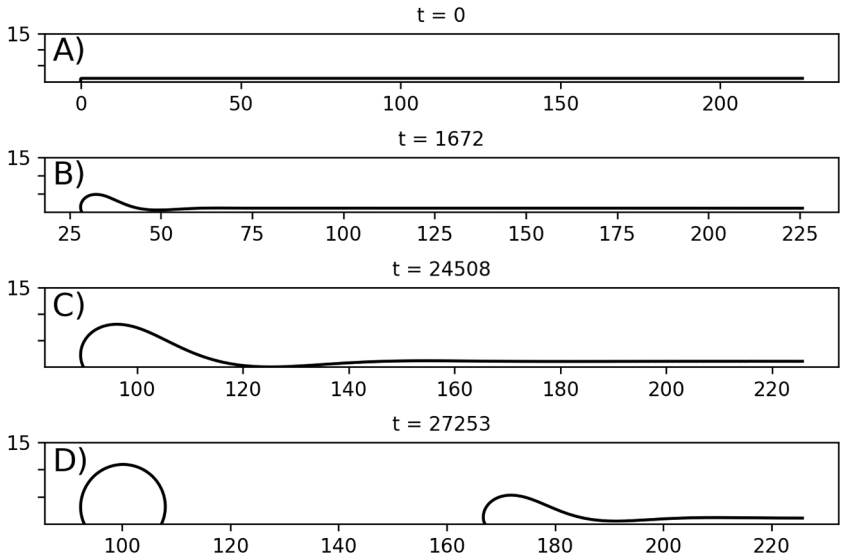

Fig. 4. Rim profile for an isotropic film with 120° contact angle as it evolves toward and through pinch-off. A) The original as-patterned edge of the film. B) Development of a rim and valley. C) At the point of pinch-off when the valley touches the substrate. This closely matches the corresponding figure 4 c) in Wong et al. [28]. Their simulations used a point-tracking method with adaptive resolution and dimensionless units such that their film had an initial thickness of 1. The simulation shown in this figure was run with resolution such that the initial film thickness was 3.5. For comparison to [28], the spatial dimensions in this figure have been divided by 3.5 and the time values have been divided by 3.5^4 (following the same non-dimensionalization of [28]). D) After pinch-off, a wire has formed and the new edge has developed a rim.

unstable perturbation. The ends of the wire began to retract and pinch off in the ovulatory manner predicted by Nichols and Mullins [23], but the middle of the wire still decomposed in a Rayleigh-like fashion.

As another demonstration of our technique, we simulated the growth of holes in isotropic films (Fig. 7). As expected, these holes maintained their initially circular shape and developed a rim with a valley behind it, as in [64]. This behavior will be contrasted with that of anisotropic films in the next section.

4.2. *Effects of anisotropy*

We applied our algorithm to anisotropic systems with facets, starting with simulations of single-crystal Ni, for which there is a large body of experimental data. Such films can be lithographically patterned with extremely long, straight edges such that in some cases these experiments can be modeled in two spatial dimensions (e.g., ignoring the dimension that runs along the edge of the film). Of particular interest is the experimental observation that for single-crystal Ni films on MgO, the edge orientations that retract most slowly are those for which the rim is bound by equilibrium facets along their length. These orientations are termed kinetically stable, because edges of other orientations will eventually facet to become composed of such edges [12]. In Ni (100) films on MgO, retracting edges with kinetically stable orientations do not exhibit the formation of a valley [5], while retracting edges with kinetically stable orientations in (110) Ni films do exhibit valley formation and pinch-off [65]. This disparity exists despite both systems having equilibrium, low-index top facets, a criterion which past simulation work suggests should be sufficient to suppress valley formation [21]. To determine if our simulation technique captures the physical behavior of this system, we first created a surface energy function based on DFT-calculated values of the surface energy for Ni [62]. For low-index orientations, this function returned the DFT-calculated value and returned a linear combination of these energies for intermediate orientations, ignoring additional energy terms for corners and edges. The cusps corresponding to equilibrium orientations were very slightly rounded to prevent $\vec{\xi}(\hat{n})$ from being ill-defined at these orientations, similar to the smoothing proposed in Bonzel and Preuss [66]. The surface energy of the (110) facet was also reduced by less than 1%, from 2.29 J/m^2 to 2.28 J/m^2 (though these quantities are effectively non-dimensional, as units are not used internally in the simulation), to ensure that this very small facet wasn't washed out by the rounding of the cusps. Viewed along the appropriate cross-section, this anisotropy function is shown in Fig. 8, which shows that despite the absence of an evident (011) cusp in $\gamma(\vec{n})$, $\vec{\xi}(\hat{n})$ still has an obvious facet. The ability of our simulation method to accommodate more complex surface anisotropy such as this is one of its core strengths. Following the lead of Jiang et al. [67], we introduced a Willmore regularization term [48], $-\varepsilon^2\left(\kappa_{ss}+\frac{1}{2}\kappa^3\right)$, to our chemical potential to give the faceting instability finite wavelength, as discussed above. In this case, ε was simply set to 1.

We then used this $\gamma(\hat{n})$ to conduct 2D edge-retraction simulations of free-standing films to isolate the effects of surface energy and diffusivity from any confounding effects of triple-line dynamics. Fig. 9 shows the results of several such simulations, with the wires cut along their long axis of symmetry for visual clarity. To test our algorithm for anisotropic diffusivity, we assigned a diffusivity value to each facet. For non-equilibrium orientations, we treated the surface as being micro-faceted and found the diffusivity through a weighted inverse sum, analogous to adding conductance in series. As in experiments, valley formation occurs in the simulations of (110) films and not in those of (100) films, even when diffusivity is isotropic. However, by manipulating the diffusivity across the (110) facet, we found that it is a key parameter for controlling the relative size of the valley that forms in (110) films. When the diffusivity across this facet is large, a deep, faceted valley develops. When this diffusivity is low, valley formation is suppressed. Fig. 9(A) and (B) contrast these two scenarios. Experimentally, valley formation is not observed in Ni (100) films [12], and it is also absent in our simulations. We attribute this to the much deeper cusp in $\gamma(\hat{n})$ associated with the (100) facets, in comparison with the (110) facets. Fig. 9(A) and (9 D) demonstrate that the experimentally observed behavior [12,65,68] of both (110) and (100) films can be accurately simulated using a single set of surface energy and diffusivity functions.

In three dimensions, experiments and simulations show that the range of phenomenology to explore is even richer, and the impact of anisotropy is even more profound. The simulation of a free-standing wire with strong anisotropy, shown in Fig. 10, demonstrates that the

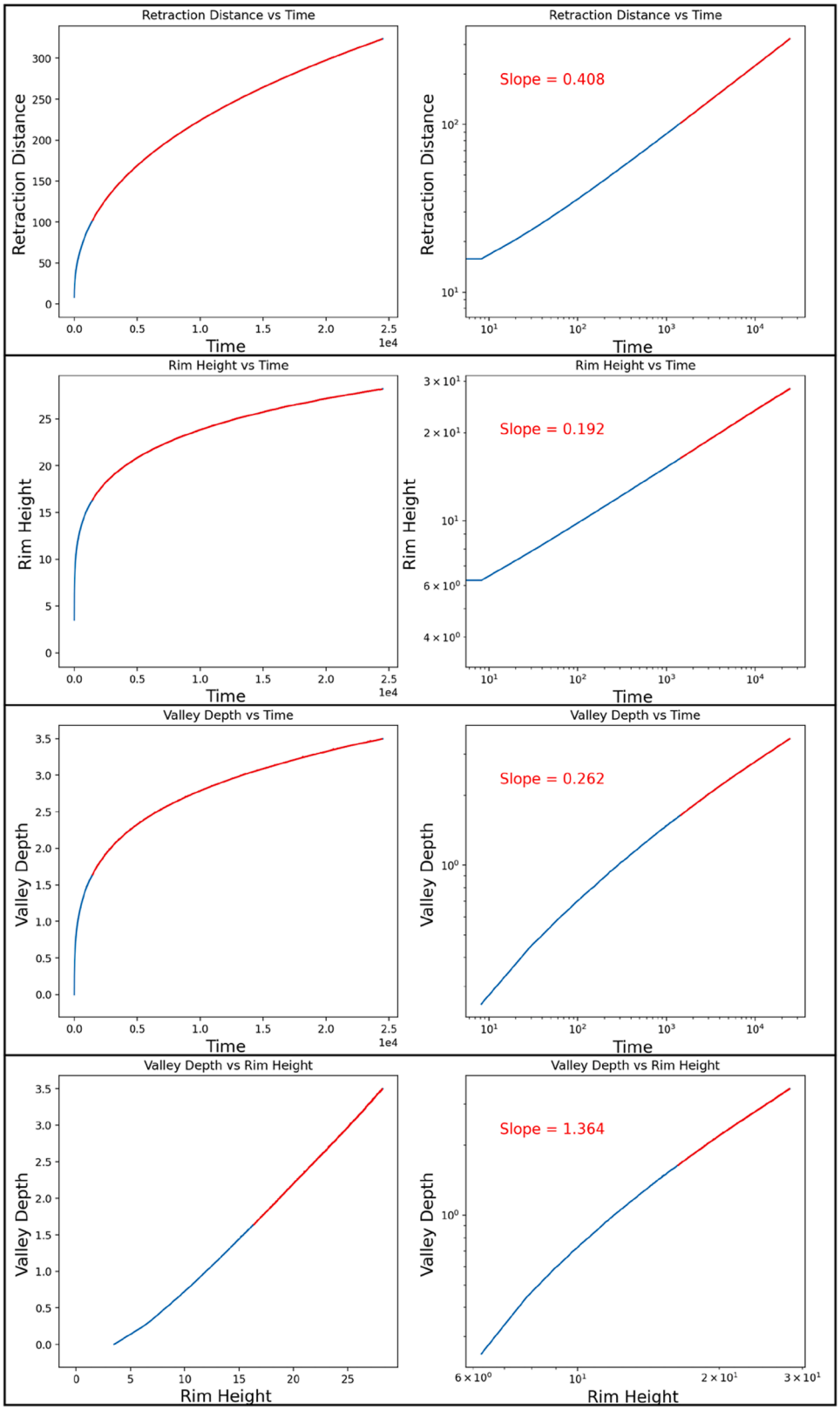

Fig. 5. Selected scaling relations for an isotropic edge retraction simulation with 90° equilibrium contact angle (Units scaled to match [28]). Data are plotted from the beginning of the simulation until just before the first pinch-off event. Log-log plots are included to show how the behavior asymptotically approaches power law scaling. The annotated least-squares-fit slope on the log-log plots corresponds to the regions highlighted in red.

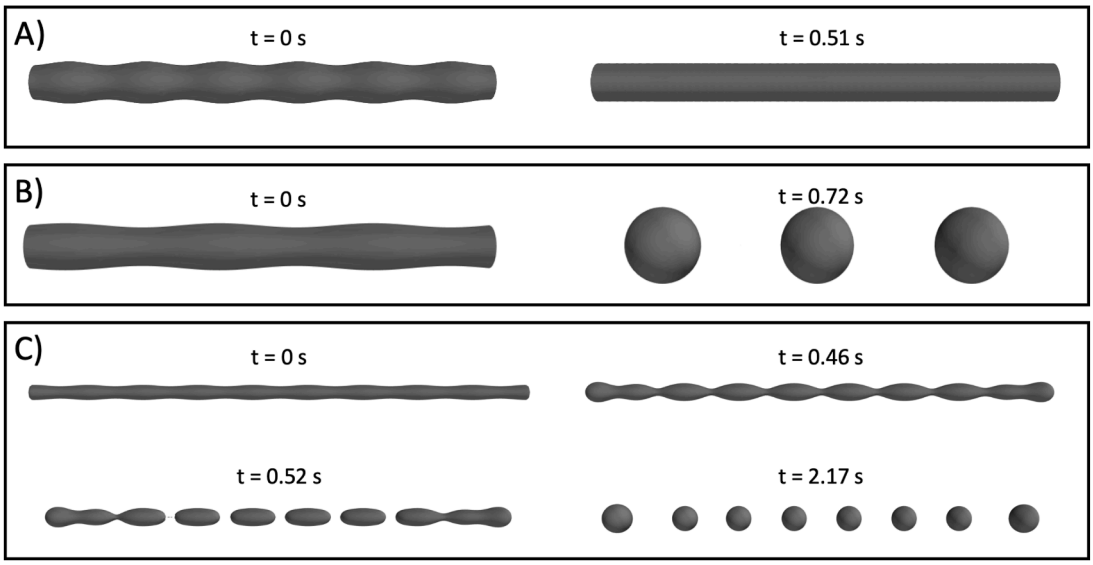

Fig. 6. Recreating the isotropic Rayleigh-like instability. A) An infinite wire with an initial perturbation of large amplitude but subcritical wavelength which decays. B) An infinite wire with an initial perturbation of the same amplitude but supercritical wavelength. This wire breaks up into spherical particles through the Rayleigh-like instability. C) A long finite wire with a perturbation of super-critical wavelength. The ends of the wire retract while the body of the wire undergoes the Rayleigh-like instability. Initial wire diameter was set to 100 nm with $D\frac{\Omega}{k_B T} = 6.2^{-21}$ m^5/J s.

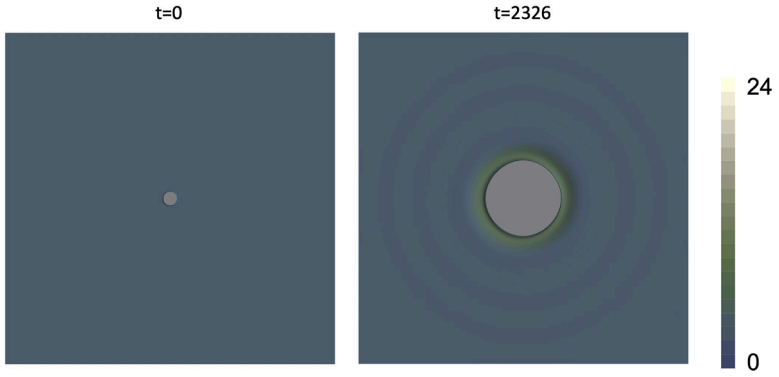

Fig. 7. An initially circular hole in an isotropic film with $\gamma_{FS} - \gamma_{VS} = 0.6$ and $\gamma_{FV} = 1$. Coloration shows variation in height.

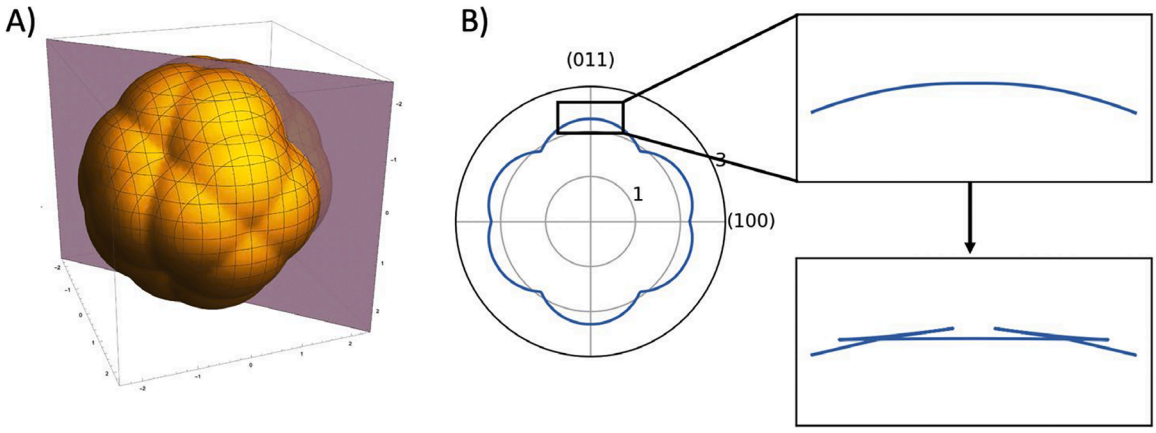

Fig. 8. A) The full surface energy function $\gamma(\hat{n})$ derived from DFT values and B) the cross-section of this function used to simulate Ni edge retraction. The insets to the right close-up plots of $\gamma(\hat{n})$ and $\overrightarrow{\xi}(\hat{n})$ in the vicinity of the (011) facet. Values are in units of J/m^2.

presence of low-energy orientations along the length of the wire can suppress the Rayleigh instability and promote ovulation. Reference [62] explores this phenomenology in detail and demonstrates strong agreement between experiment and simulations using this technique. Reference [69] also demonstrates that strong anisotropy can suppress both the Rayleigh instability and ovulation in wires with special,

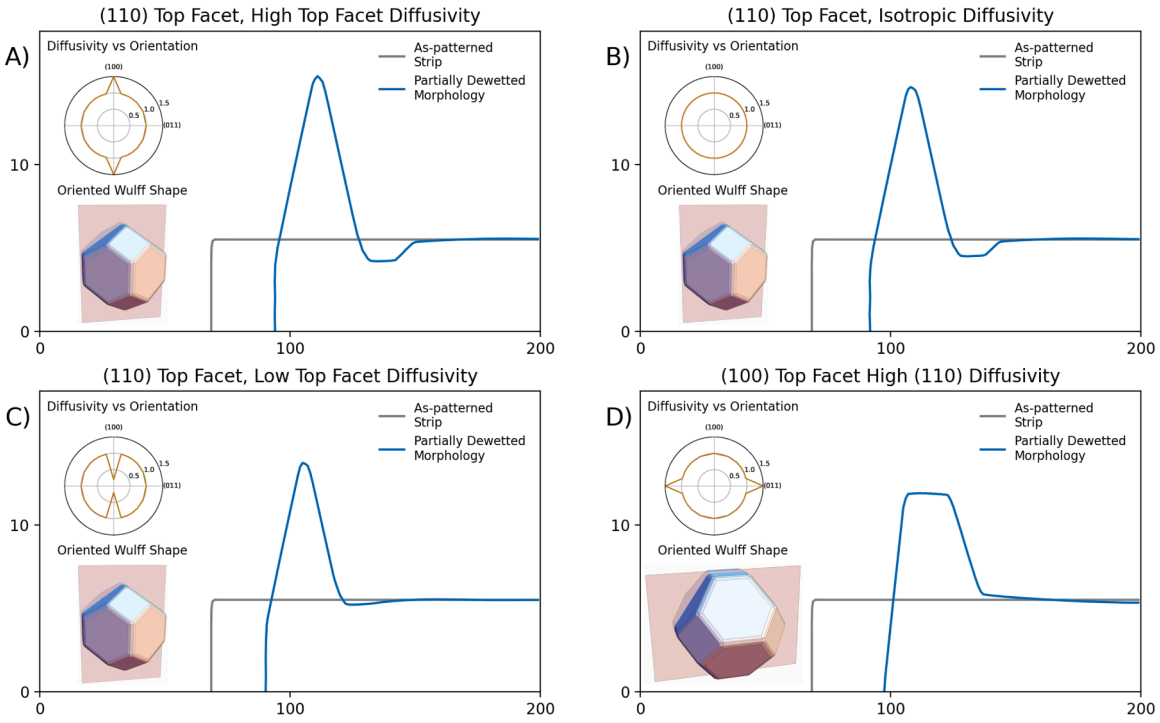

Fig. 9. 2D simulations of retracting film edges. Note very different x and y scales. Full wires were 360 units long to start and 11 units tall. As discussed in the text, the films in these simulations are free-standing to avoid confounding substrate effects. Only the top half of the wires is shown because the simulation is symmetric in this direction. A) Most closely matches experiments [12] [59],[62, Ch. 6], and D) shows that experimental behavior (suppressed valley formation) in (100) films can be reproduced using the same parameters as A). The upper-left corner of each subplot shows the diffusivity function used in the simulation, while the lower-left corner shows how the orientation of the strip corresponds to the equilibrium Wulff-shape (based on the function shown in Fig. 6 (a-c)).

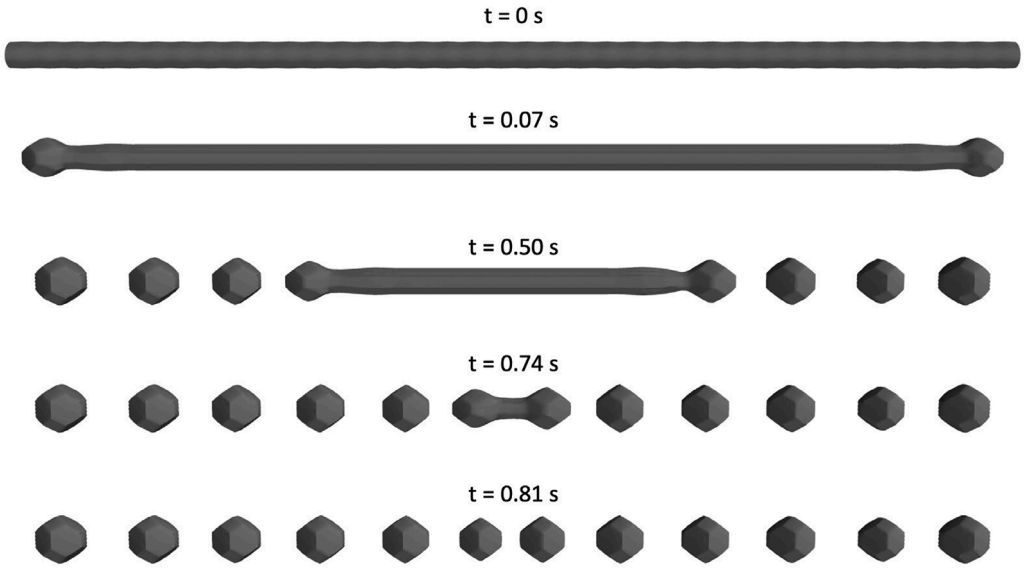

Fig. 10. Long Ni wire with short wavelength perturbation. Wire is bound by (001) and (011) -type facets along its length. These facets suppress the Rayleigh-like instability but allow for ovulation. Initial wire diameter was set to 100 nm with $D\frac{\Omega}{k_B T} = 6.2^{-21}$ m^5/J s for all $\hat{n}$.

high-stability orientations. In the simulation shown in Fig. 10, $\vec{\xi}(\hat{n})$ was again based on the same DFT values as above, although only the three lowest energy families of facets—(001), (011), and (111)—were used and they were configured to have small spinodes at all corners and edges.

Another example of this simulation technique recovering complex, anisotropic behavior is shown in Fig. 11. In this simulation, a film with a (100) top surface is initialized with a circular hole. However, this hole quickly grows to its kinetic Wulff shape [7,11] which in this case is bound by long edges with [110] in-plane normals and truncated corners with [100] in-plane normals. As the hole continues to grow, a corner instability develops [17], yielding behavior with striking resemblance to experimental observations [5,17]. To reduce the size of the simulation domain, only one quadrant of the film was simulated, and mirror boundary conditions were used. This simulation was conducted using the same $\vec{\xi}(\hat{n})$ as the simulation in Fig. 10, with mirror boundary

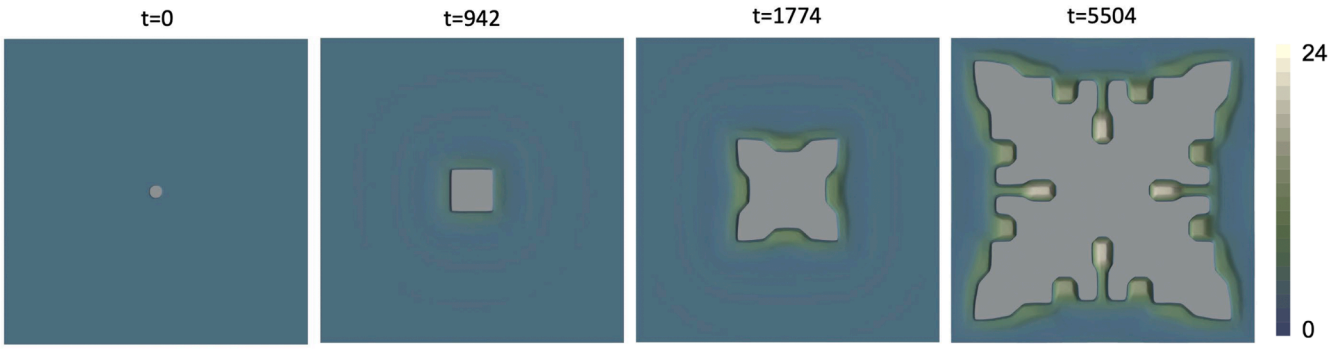

Fig. 11. An initially circular hole in a simulated Ni film. The hole first grows to reach its kinetic Wulff shape before developing the corner instability. The corners eventually begin to exhibit dendrite-like morphology. Coloration shows variation in height.

conditions used on the right side of the wire. The film-substrate interfacial energy was set to 0.6 J/m^2, to roughly correspond to the partially non-wetting behavior seen in past studies of Ni (100) films on MgO.

5. Future work

The code developed for this work, available as a complete example simulation on Github, was designed with a high degree of modularity, with an eye toward future improvements to physical accuracy and performance. As with any simulation method, the degree to which this technique reproduces physical reality is limited by the accuracy of the materials properties used as input. We chose to base our definition of $\vec{\xi}(\hat{n})$ around DFT-derived surface energy values because such values are useful proxies for the underlying structure of the material and are readily available for a wide-variety of materials at http://crystalium.materialsvirtuallab.org/ [62]. While these relatively simplistic models were evidently sufficient to yield simulation results that recover experimental observations, they are far from perfect. They do not, for example, take into account changes in surface free energy with temperature. More realistic models of surface energy anisotropy, across a range of temperatures, can be calculated using molecular dynamics [70], and such values could be directly plugged into the modeling method presented here, since any arbitrary $\vec{\xi}(\hat{n})$ can be represented as a lookup table. Such an approach could allow an investigation into how changes in temperature, including thermal roughening of high-energy facets, impact dewetting behavior. From a performance standpoint, this code has been optimized to the point where its calls to the scikit-fmm package are now the rate limiting steps. We think it should be possible to write a new implementation of the velocity extension algorithm which allows multiple quantities (in this case, κ_γ and v_n) to be extended without repeating redundant fast marching computations. We anticipate that this could yield a roughly 3x boost in performance, perhaps more if the implementation is also written in Julia to eliminate the overhead of calls to Python-wrapped C-code. Another area of future work could be to use an adaptive simulation grid which locally increases the resolution of the simulation in regions of high curvature. We also believe there are likely better ways to suppress the formation of non-physical sawtooth surfaces than penalizing $\nabla^2\phi(\vec{x})$, as we did here. Still, as demonstrated, this code already has sufficient performance and accuracy to probe many physical phenomena of interest in reasonable amounts of time.

6. Conclusions

The $\vec{\xi}(\hat{n})$ level-set method of simulating morphological evolution proposed and demonstrated above is capable of reproducing experimental results with a high degree of fidelity. This method is capable of handling surface energy functions with hard anisotropy in conjunction with anisotropic surface self-diffusivity. Critically, this method overcomes the numerical stability and volume conservation issues which are common in level-set simulations of high-order PDEs. The method uses $\nabla\cdot\vec{\xi}(\hat{n})$ to compute the weighted mean curvature which combines surface tension with geometry to produce the position-dependent surface-potential. The normal velocity $\vec{v}(\vec{x},t)$ is computed from the surface Laplacian of weighted mean curvature. Incorporation of redistancing and velocity extension algorithms produces enhanced numerical stability and allows our method to achieve volume conservation within a few percent while maintaining the benefits of the level-set method, such as natural handling of topological changes. We have shown that our method matches known behavior for the isotropic Rayleigh instability and edge retraction. In addition, it matches behavior observed in experiments in which anisotropy plays a central role, including the orientational dependence of valley formation ahead of retracting edges and the development of faceted holes that undergo a corner instability. Our software for simulating morphological evolution caused by anisotropic surface diffusion is available on Github. This software will enable new research on solid-state dewetting, including advances in understanding that will aid in the use of solid state dewetting to obtain specific morphologies useful in micro- and nano-scale devices.

CRediT authorship contribution statement

Maxwell A. L'Etoile: Writing – review & editing, Writing – original draft, Visualization, Software, Methodology, Investigation, Conceptualization. **Carl V. Thompson:** Writing – review & editing, Supervision, Project administration, Funding acquisition, Conceptualization. **W. Craig Carter:** Writing – review & editing, Visualization, Supervision, Software, Methodology, Conceptualization.

Declaration of competing interest

The authors declare that they have no known competing financial interests or personal relationships that could have appeared to influence the work reported in this paper.

Acknowledgements

This work was supported by NSF Grant Nos. DMR-1505947 and EECS-1740274.

Appendices

A. Numerical details

In broad strokes, we integrate our governing equation forward in time by first taking the required spatial derivatives of ϕ using narrow-banded second-order central differences. From these derivatives, the normal vector of the surface is computed within a narrow band around the surface, and this normal vector is used to compute the weighted mean curvature, as detailed in the Methods section. This weighted mean curvature is extended away from the surface using fast-marching methods and is subsequently used to calculate the surface velocity, according to the Mullins equation, again using second-order central differences for all spatial derivatives. This velocity is also extended away from the surface using fast-marching methods, and the size of the time step to use is computed, as detailed in the Methods section, taking into account the maximum surface velocity. The governing equation is then integrated one time step forward using the calculated velocity and step size. These steps are repeated in a loop, with redistancing occurring either after every time step for 3D simulations, or periodically for 2D simulations. As mentioned in the main text, a simple 3D example is available on Github.

B. Computational performance

Our implementation of this simulation method was written in the Julia programming language [64] which enables high performance code that is easy to write and read. The most computationally intensive parts of our code have been parallelized, and for the size of simulations demonstrated here, overall performance saturates when 3 threads are used in 2D and 6 threads are used in 3D. This is because the fast-marching package we use, scikit-fmm, is single-threaded and calls to its fast marching and velocity extension functions become rate limiting for the simulation. We have mitigated this issue through the use of scikit-fmm's ability to only update points in a narrow band around the $\phi = 0$ level-set. We run our code on a workstation computer with a 2019-era AMD Threadripper CPU. The 2D simulations shown here take tens of hours to complete while the 3D simulations can take several days. Code that runs faster would allow for higher resolution simulations within reasonable times. The resolution of the simulation limits the size of facets that can be resolved, and simulations with resolution that is too low suffer from poor volume conservation and missing details. Potential approaches for improving computational performance are discussed in the Future Work section of the main text.

References

[1] R. Brandon, F.J. Bradshaw, The mobility of the surface atoms of copper and silver evaporated deposits. Royal Aircraft Establishment Farnborough (United Kingdom), 1966. https://apps.dtic.mil/docs/citations/AD0638210 (accessed June 11, 2021).

[2] E. Jiran, C.V. Thompson, Capillary Instabilities in Thin Films film, J. Electron. Mater. 19 (1990) 1153–1160.

[3] P.R. Gadkari, A.P. Warren, R.M. Todi, R.V. Petrova, K.R. Coffey, Comparison of the agglomeration behavior of thin metallic films on SiO2, J. Vac. Sci. Technol. Vac. Surf. Films 23 (2005) 1152–1161, https://doi.org/10.1116/1.1861943.

[4] R. Nuryadi, Y. Ishikawa, M. Tabe, Formation and ordering of self-assembled Si islands by ultrahigh vacuum annealing of ultrathin bonded silicon-on-insulator structure, Appl. Surf. Sci. 159–160 (2000) 121–126, https://doi.org/10.1016/S0169-4332(00)00051-9.

[5] J. Ye, C.V. Thompson, Mechanisms of complex morphological evolution during solid-state dewetting of single-crystal nickel thin films, Appl. Phys. Lett. 97 (2010) 071904, https://doi.org/10.1063/1.3480419.

[6] E. Rabkin, D. Amram, E. Alster, Solid state dewetting and stress relaxation in a thin single crystalline Ni film on sapphire, Acta Mater 74 (2014) 30–38, https://doi.org/10.1016/J.ACTAMAT.2014.04.020.

[7] R.W. Balluffi, S.M. Allen, W.C. Carter, Surface evolution due to capillary forces, Kinet. Mater. (2005). https://ui.adsabs.harvard.edu/abs/2005kima.book.....B (accessed January 11, 2022).

[8] C.V. Thompson, Solid-state dewetting of thin films, Annu. Rev. Mater. Res. 42 (2012) 399–434, https://doi.org/10.1146/annurev-matsci-070511-155048.

[9] E. Bussmann, F. Cheynis, F. Leroy, P. Müller, O. Pierre-Louis, Dynamics of solid thin-film dewetting in the silicon-on-insulator system, New J. Phys. 13 (2011) 043017, https://doi.org/10.1088/1367-2630/13/4/043017.

[10] J. Ye, D. Zuev, S. Makarov, Dewetting mechanisms and their exploitation for the large-scale fabrication of advanced nanophotonic systems FULL CRITICAL REVIEW Dewetting mechanisms and their exploitation for the large-scale fabrication of advanced nanophotonic systems, (2018). https://doi.org/10.1080/09506608.2018.1543832.

[11] J. Ye, C.V. Thompson, Anisotropic edge retraction and hole growth during solid-state dewetting of single crystal nickel thin films, Acta Mater 59 (2011) 582–589, https://doi.org/10.1016/j.actamat.2010.09.062.

[12] G.Hyun Kim, R.V. Zucker, J. Ye, W.Craig Carter, C.V. Thompson, Quantitative analysis of anisotropic edge retraction by solid-state dewetting of thin single crystal films, J. Appl. Phys. 113 (2013) 043512, https://doi.org/10.1063/1.4788822.

[13] G.H. Kim, C.V. Thompson, Effect of surface energy anisotropy on Rayleigh-like solid-state dewetting and nanowire stability, Acta Mater 84 (2015) 190–201, https://doi.org/10.1016/J.ACTAMAT.2014.10.028.

[14] F. Leroy, F. Cheynis, T. Passanante, P. Müller, Dynamics, anisotropy, and stability of silicon-on-insulator dewetting fronts, Phys. Rev. B 85 (2012) 195414, https://doi.org/10.1103/PhysRevB.85.195414.

[15] Y.A. Shin, C.V. Thompson, Templated fingering during solid state dewetting, Acta Mater 207 (2021) 116669, https://doi.org/10.1016/j.actamat.2021.116669.

[16] F. Leroy, F. Cheynis, T. Passanante, P. Müller, Influence of facets on solid state dewetting mechanisms: comparison between Ge and Si on ${\mathbf{SiO}}_{\mathbf{2}}$, Phys. Rev. B 88 (2013) 035306 https://doi.org/10.1103/PhysRevB.88.035306.

[17] R.V. Zucker, G.H. Kim, J. Ye, W.C. Carter, C.V. Thompson, The mechanism of corner instabilities in single-crystal thin films during dewetting, J. Appl. Phys. 119 (2016) 125306, https://doi.org/10.1063/1.4944712.

[18] W.W. Mullins, Theory of thermal grooving, J. Appl. Phys. 28 (1957) 333–339, https://doi.org/10.1063/1.1722742.

[19] P. Smereka, Semi-implicit level set methods for curvature and surface diffusion motion, 2003.

[20] J.E. Taylor, II-mean curvature and weighted mean curvature, Acta Metall. Mater. 40 (1992) 1475–1485, https://doi.org/10.1016/0956-7151(92)90091-R.

[21] R.V. Zucker, G.H. Kim, W.Craig Carter, C.V. Thompson, A model for solid-state dewetting of a fully-faceted thin film, Comptes Rendus Phys 14 (2013) 564–577, https://doi.org/10.1016/J.CRHY.2013.06.005.

[22] G.H. Kim, Study of Phenomenologies During Templated Solid-State Dewetting of Thin Single Crystal films, Thesis, Massachusetts Institute of Technology, 2016. https://dspace.mit.edu/handle/1721.1/103184 (accessed January 11, 2022).

[23] F.A. Nichols, W.W. Mullins, Morphological changes of a surface of revolution due to capillarity-induced surface diffusion, J. Appl. Phys. 36 (1965) 1826–1835, https://doi.org/10.1063/1.1714360.

[24] F.A. Nichols, W.W. Mullins, Surface- (Interface-) and volume diffusion contributions to morophological changes driven by capillarity, Trans. Metall. Soc. AIME 233 (1965) 1840–1847.

[25] Lord Rayleigh, On the instability of jets, Proc. Lond. Math. Soc. s1-10 (1878) 4–13, https://doi.org/10.1112/plms/s1-10.1.4.

[26] M.S. Mccallum, P.W. Voorhees, M.J. Miksis, S.H. Davis, H. Wong, Capillary instabilities in solid thin films: lines, J. Appl. Phys. 79 (1996) 7604, https://doi.org/10.1063/1.362343.

[27] W.C. Carter, A.M. Glaeser, The morphological stability of continuous intergranular phases: thermodynamic considerations, Acta Metall 35 (1987) 237–245, https://doi.org/10.1016/0001-6160(87)90231-8.

[28] H. Wong, P.W. Voorhees, M.J. Miksis, S.H. Davis, Periodic mass shedding of a retracting solid film step, Acta Mater 48 (2000) 1719–1728, https://doi.org/10.1016/S1359-6454(00)00016-1.

[29] R.V. Zucker, W.C. Carter, C.V. Thompson, Power-law scaling regimes for solid-state dewetting of thin films, Scr. Mater. 116 (2016) 143–146, https://doi.org/10.1016/j.scriptamat.2016.01.039.

[30] F.A. Nichols, On the spheroidization of rod-shaped particles of finite length, J. Mater. Sci. 11 (1976) 1077–1082, https://doi.org/10.1007/BF00553115.

[31] W. Jiang, W. Bao, C.V. Thompson, D.J. Srolovitz, Phase field approach for simulating solid-state dewetting problems, Acta Mater 60 (2012) 5578–5592, https://doi.org/10.1016/J.ACTAMAT.2012.07.002.

[32] A.R. Roosen, J.E. Taylor, Modeling crystal growth in a diffusion field using fully faceted interfaces, J. Comput. Phys. 114 (1994) 113–128, https://doi.org/10.1006/jcph.1994.1153.

[33] A.R. Roosen, W.C. Carter, Simulations of microstructural evolution: anisotropic growth and coarsening, Phys. Stat. Mech. Its Appl. 261 (1998) 232–247, https://doi.org/10.1016/S0378-4371(98)00377-X.

[34] C.M. Bishop, R.L. Satet, R.M. Cannon, W.C. Carter, A.R. Roosen, A simple model of fully-faceted grain growth and coarsening with non-linear growth laws, Z. Für Met. 96 (2005) 124–134.
[35] E. Dornel, J.C. Barbé, F. De Crécy, G. Lacolle, J. Eymery, Surface diffusion dewetting of thin solid films: numerical method and application to Si/SiO2, Phys. Rev. B - Condens. Matter Mater. Phys. 73 (2006) 1–10, https://doi.org/10.1103/PhysRevB.73.115427.
[36] M. Burger, F. Haußer, C. Stöcker, A. Voigt, A level set approach to anisotropic flows with curvature regularization, J. Comput. Phys. 225 (2007) 183–205, https://doi.org/10.1016/j.jcp.2006.11.026.
[37] W. Jiang, Q. Zhao, W. Bao, Sharp-Interface Approach for Simulating Solid-State Dewetting in Three Dimensions, 2019. http://arxiv.org/abs/1902.05272 (accessed December 16, 2019).
[38] W. Jiang, Q. Zhao, Sharp-interface approach for simulating solid-state dewetting in two dimensions: a Cahn–Hoffman ξ-vector formulation, Phys. Nonlinear Phenom. 390 (2019) 69–83, https://doi.org/10.1016/j.physd.2018.11.003.
[39] O. Pierre-Louis, A. Chame, Y. Saito, Dewetting of a Solid Monolayer, (2007). https://doi.org/10.1103/PhysRevLett.99.136101.
[40] O. Pierre-Louis, A. Chame, M. Dufay, Atomic step motion during the dewetting of ultra-thin films, Eur. Phys. J. B 77 (2010) 57–63, https://doi.org/10.1140/epjb/e2010-00253-8.
[41] O. Pierre-Louis, A. Chame, Y. Saito, Dewetting of Ultrathin Solid Films, Phys. Rev. Lett. 103 (2009) 195501, https://doi.org/10.1103/PhysRevLett.103.195501.
[42] N. Wang, A. Karma, Fragmentation of faceted crystalline wires, Phys. Rev. Mater. 6 (2022) 106002, https://doi.org/10.1103/PhysRevMaterials.6.106002.
[43] H.-Z. Yuan, C. Shu, Y. Wang, S. Shu, A simple mass-conserved level set method for simulation of multiphase flows, Phys. Fluids 30 (2018) 040908, https://doi.org/10.1063/1.5010152.
[44] Z. Solomenko, P.D.M. Spelt, L. Ó Náraigh, P. Alix, Mass conservation and reduction of parasitic interfacial waves in level-set methods for the numerical simulation of two-phase flows: a comparative study, Int. J. Multiph. Flow 95 (2017) 235–256, https://doi.org/10.1016/j.ijmultiphaseflow.2017.06.004.
[45] M. Sussman, E.G. Puckett, A coupled level set and volume-of-fluid method for computing 3d and axisymmetric incompressible two-phase flows, J. Comput. Phys. 162 (2000) 301–337, https://doi.org/10.1006/jcph.2000.6537.
[46] D.W. Hoffman, J.W. Cahn, A vector thermodynamics for anisotropic surfaces. I. Fundamentals and application to plane surface junctions, Surf. Sci. 31 (1972) 368–388, https://doi.org/10.1016/0039-6028(72)90268-3.
[47] J.W. Cahn, W.C. Carter, Crystal shapes and phase equilibria: a common mathematical basis, Metall. Mater. Trans. A (n.d.) 10.
[48] T.J. Willmore, Riemannian Geometry, Oxford University Press, 1993.
[49] S. Angenent, M.E. Gurtin, Multiphase thermomechanics with interfacial structure 2. Evolution of an isothermal interface, Arch. Ration. Mech. Anal. 108 (1989) 323–391.
[50] B. Li, J. Lowengrub, A. Rätz, A. Voigt, Review article: geometric evolution laws for thin crystalline films: modeling and numerics, Commun Comput Phys 6 (2009) 433–482.
[51] J.E. Hilliard, J.W. Cahn, On the nature of the interface between a solid metal and its melt, Acta Metall 6 (1958) 772–774, https://doi.org/10.1016/0001-6160(58)90052-X.
[52] S.M. Allen, J.W. Cahn, A microscopic theory for antiphase boundary motion and its application to antiphase domain coarsening, Acta Metall 27 (1979) 1085–1095, https://doi.org/10.1016/0001-6160(79)90196-2.
[53] F. Almgren, Questions and answers about area-minimizing surfaces and geometric measure theory, in: R.E. Greene, S.-T. Yau (Eds.), Differ. Geom. Partial Differ. Equ. Manifolds, American Mathematical Soc., 1993.
[54] S. Osher, J.A. Sethian, Fronts propagating with curvature-dependent speed: algorithms based on Hamilton-Jacobi formulations, J. Comput. Phys. 79 (1988) 12–49, https://doi.org/10.1016/0021-9991(88)90002-2.
[55] H.K. Zhao, T. Chan, B. Merriman, S. Osher, A variational level set approach to multiphase motion, J. Comput. Phys. 127 (1996) 179–195, https://doi.org/10.1006/jcph.1996.0167.
[56] D. Adalsteinsson, J.A. Sethian, The fast construction of extension velocities in level set methods, J. Comput. Phys. 148 (1999) 2–22, https://doi.org/10.1006/jcph.1998.6090.
[57] J.A. Sethian, A fast marching level set method for monotonically advancing fronts, Proc. Natl. Acad. Sci. 93 (1996) 1591–1595, https://doi.org/10.1073/pnas.93.4.1591.
[58] J. Furtney, scikit-fmm: the Fast Marching Method for Python, 2021. https://github.com/scikit-fmm/scikit-fmm (accessed January 10, 2022).
[59] M. Sussman, E. Fatemi, S.J.C. Sci, An efficient, Interface-Preserving Level Set Redistancing Algorithm and Its Application to Interfacial Incompressible Fluid Flow, 1999. http://www.siam.org/journals/ojsa.php (accessed January 13, 2020).
[60] K. Khedkar, A.C. Mamaghani, P. Ghysels, N.A. Patankar, A.P.S. Bhalla, Preventing mass loss in the standard level set method: new insights from variational analyses, (2024). https://doi.org/10.48550/arXiv.2404.03132.
[61] J. Smith, G. Petrova, S. Schaefer, Encoding normal vectors using optimized spherical coordinates. Comput. Graph. Pergamon, Elsevier Ltd, 2012, pp. 360–365, https://doi.org/10.1016/j.cag.2012.03.017.
[62] R. Tran, Z. Xu, B. Radhakrishnan, D. Winston, W. Sun, K.A. Persson, S.P. Ong, Surface energies of elemental crystals, Sci. Data 3 (2016) 160080, https://doi.org/10.1038/sdata.2016.80.
[63] M. Khenner, A. Averbuch, M. Israeli, M. Nathan, Numerical simulation of grain-boundary grooving by level set method, J. Comput. Phys. 170 (2001) 764–784, https://doi.org/10.1006/jcph.2001.6760.
[64] D.J. Srolovitz, S.A. Safran, Capillary instabilities in thin films. II. Kinetics, J. Appl. Phys. 60 (1986) 255–260, https://doi.org/10.1063/1.337691.
[65] J. Ye, C.V. Thompson, Regular pattern formation through the retraction and pinch-off of edges during solid-state dewetting of patterned single crystal films, Phys. Rev. B - Condens. Matter Mater. Phys. 82 (2010) 1–4, https://doi.org/10.1103/PhysRevB.82.193408.
[66] H.P. Bonzel, E. Preuss, Morphology of periodic surface profiles below the roughening temperature: aspects of continuum theory, Surf. Sci. 336 (1995) 209–224, https://doi.org/10.1016/0039-6028(95)00508-0.
[67] W. Jiang, Y. Wang, Q. Zhao, D.J. Srolovitz, W. Bao, Solid-state dewetting and island morphologies in strongly anisotropic materials, Scr. Mater. 115 (2016) 123–127, https://doi.org/10.1016/j.scriptamat.2016.01.018.
[68] Y.A. Shin, Templated Solid-State Dewetting of Single Crystal Ni Thin Films, Massachusetts Institute of Technology, 2022.
[69] M.A. L'Etoile, B. Wang, Q. Cumston, A.P. Warren, J.C. Ginn, K. Barmak, K. R. Coffey, W.C. Carter, C.V. Thompson, Experimental and computational study of the orientation dependence of single-crystal ruthenium nanowire Stability, Nano Lett 22 (2022) 9958–9963, https://doi.org/10.1021/acs.nanolett.2c03529.
[70] J.J. Hoyt, M. Asta, A. Karma, Method for computing the anisotropy of the solid-liquid interfacial free energy, Phys. Rev. Lett. 86 (2001) 5530–5533, https://doi.org/10.1103/PhysRevLett.86.5530.
[71] M.A. L'Etoile, mletoile/surface-self-diffusion, (2024). https://github.com/mletoile/surface-self-diffusion (accessed September 27, 2024).